PHYSICAL REVIEW E **95**, 062415 (2017)

Backward renormalization-group inference of cortical dipole sources and neural connectivity efficacy

Selene da Rocha Amaral[*]
Instituto de Física, Universidade Federal de Goiás, CEP 74690-900, Goiânia-Go, Brazil

Luiz A. Baccalá[†]
Dep. de Telecomunicações e Controle, Escola Politécnica, Universidade de São Paulo, CEP 05508-900, São Paulo-SP, Brazil

Leonardo S. Barbosa[‡] and Nestor Caticha[§]
Dep. de Física Geral, Instituto de Física, Universidade de São Paulo, CEP 66318, 05315-970, São Paulo-SP, Brazil

(Received 28 January 2017; revised manuscript received 5 May 2017; published 23 June 2017)

Proper neural connectivity inference has become essential for understanding cognitive processes associated with human brain function. Its efficacy is often hampered by the curse of dimensionality. In the electroencephalogram case, which is a noninvasive electrophysiological monitoring technique to record electrical activity of the brain, a possible way around this is to replace multichannel electrode information with dipole reconstructed data. We use a method based on maximum entropy and the renormalization group to infer the position of the sources, whose success hinges on transmitting information from low- to high-resolution representations of the cortex. The performance of this method compares favorably to other available source inference algorithms, which are ranked here in terms of their performance with respect to directed connectivity inference by using artificially generated dynamic data. We examine some representative scenarios comprising different numbers of dynamically connected dipoles over distinct cortical surface positions and under different sensor noise impairment levels. The overall conclusion is that inverse problem solutions do not affect the correct inference of the direction of the flow of information as long as the equivalent dipole sources are correctly found.

DOI: 10.1103/PhysRevE.95.062415

I. INTRODUCTION

A major step in understanding the mechanisms underlying brain function deals with modeling its electromagnetic properties. Neural activity and its associated ionic dipole currents give rise to externally measurable potentials or fields. Calculation of dipole current external manifestations such as scalp potentials constitutes the forward problem. This is already a reasonably hard problem due to the convoluted geometry of the brain and the conduction discontinuities in the head, which determine its Green's function. More demanding is the inverse problem, i.e., to obtain estimates of the dipole currents, given the external measurements. We address the inverse problem, the inference of the dipole currents, by using maximum entropy and the renormalization group. We then go on to study whether, from the inferred currents, the information flow between different regions can also be determined in what is termed the neural connectivity problem. Different types of neural connectivity can be considered, such as structural (i.e., anatomical), functional, and effective connectivity [1], which, even though they have been introduced in the brain analysis context, can also be used whenever characterizing multiple time series interactions. In view of the ever-growing realization that adequate connectivity descriptions are essential to understand the mechanisms behind brain function, whether under normal or under pathological conditions, research efforts have been focused towards including connectivity characterization as a goal [2–4]. The popularity of current methods varies according to brain signal modality (scalp electroencephalogram (EEG), brain field potentials, functional magnetic resonance imaging (fMRI), action potential characterization, magnetoencephalography (MEG) [2–9]). While on one hand, adequate connectivity inference requires including the dynamics of as many simultaneous structures as possible, the statistical estimation performance of all methods is severely penalized as the number of structures that need to be considered grows. Efforts at circumventing this are geared to dimensionality reduction strategies. Broadly speaking, achieving dimensionality reduction amounts to representing the data through some minimal set of relevant observations or parameters. Here we focus on how to reduce the number of time series that need to be processed when dealing with EEG. Substantial work has been done both in what is termed the EEG electrode space [10,11] (using electrode data directly) and the region of interest (ROI) space, i.e., one based on employing signals obtained by solving the inverse problem of source reconstruction [12–14]. Suppose that the cortex is represented at a certain resolution by a lattice of points, typically of the order of 10^5. Then in principle any site could be a source or sink of information. By working only with a few identified active sites the dimensional reduction can be effectively achieved. This represents an advantage over working on the space of electrodes for two reasons. One is that a reduction from $O(10^2)$ electrode time series to a few active region time series is achieved. Second, and maybe more importantly from a biological point of view, connectivity between active sources is potentially more informative than between scalp electric potentials.

---

[*] seleneramaral@gmail.com
[†] baccala@lcs.poli.usp.br
[‡] leonardo.barbosa@pobox.com
[§] nestor@if.usp.br

By their very own nature source reconstruction problems are mathematically ill posed [15]. This implies considerable uncertainty regarding achievable solutions. Despite this, a fair level of signal characterization success has been achieved in source or neural activity characterization. This stands in marked contrast to much rarer systematic ROI-based connectivity method appraisals [16–18]. To help extend the breadth of those appraisals we examine different source reconstruction techniques under partial directed coherence (PDC) [2] connectivity inference. PDC was chosen because it is a frequency domain quantifier of the concept of Granger causality [19] (see Appendix C for more details) and because EEG spectral bands reflect important neurophysiological states [20]. An additional consideration for selecting PDC was its established asymptotic statistical criteria for inferring connections [21]. For the inverse problem, three popular source localization estimation techniques, variational Bayes (VB) [22], standardized Loreta (sLoreta) [23,24], and minimum norm estimate (MNE) [25], are considered together with a recently introduced method to deal with the crucial step of determining a prior. This last method of inference, which works at several different scales, is divided into two parts. First, the inference part leads from a prior distribution of sources to a posterior distribution, on a given scale. The second part leads from a posterior on a coarse scale to a prior on a refined scale using renormalization group (RG) ideas. Here we use a variational Bayes method for the inference part and hence the resulting algorithm is termed backward renormalization group variational Bayes (BRG-VB). The BRG method was presented in Ref. [26] and it draws from ideas in Refs. [28,29]. In practice ROI space performance is important because all connectivity estimation methods are limited by the number of time series that need to be simultaneously considered thus making adequate ROI estimation a potentially useful means of dimensionality reduction as mentioned before. We have used artificial data simulations to rank the reconstruction methods with respect to correct connectivity inference.

This paper is organized as follows. Section II describes the forward problem of generating the scalp potential time series. This permits generating artificial data from any desired distribution of dipole currents. In Sec. III the inverse problem is described and the BRG method as applied to EEG is discussed. Section IV presents the method to, first, obtain interacting time series, which will act as dipole current sources and, second, how to estimate the causal interactions between these sources. In Sec. V we show the results of applying these methods to different configurations of interacting series and a discussion appears in Sec. VI together with ensuing conclusions.

II. FORWARD PROBLEM

There are several possibilities of how the cortex can be represented by a discrete lattice. The highest-resolution lattice, where the centroid of each triangular face represents one current dipole, is Λ_D [Fig. 1(e)] and has $|\Lambda_D| \approx 10^4$ triangular plaquettes. This is an approximate representation of the continuum limit, represented by a lattice Λ_c of $O(10^5)$ sites obtained from a structural magnetic resonance image (MRI) for each hemisphere [30]. Notice that the space where the forward problem will live depends on assumptions made about plausible sources and sinks of current in the brain. Most of the current passing through EEG sensors (and magnetic field flowing thought MEG sensors) is assumed to stem from large pyramidal cells located in the third layer of the cortical mantle. Tens of thousands of neurons aligned in columnar structures generate a dipole moment that dominates the current

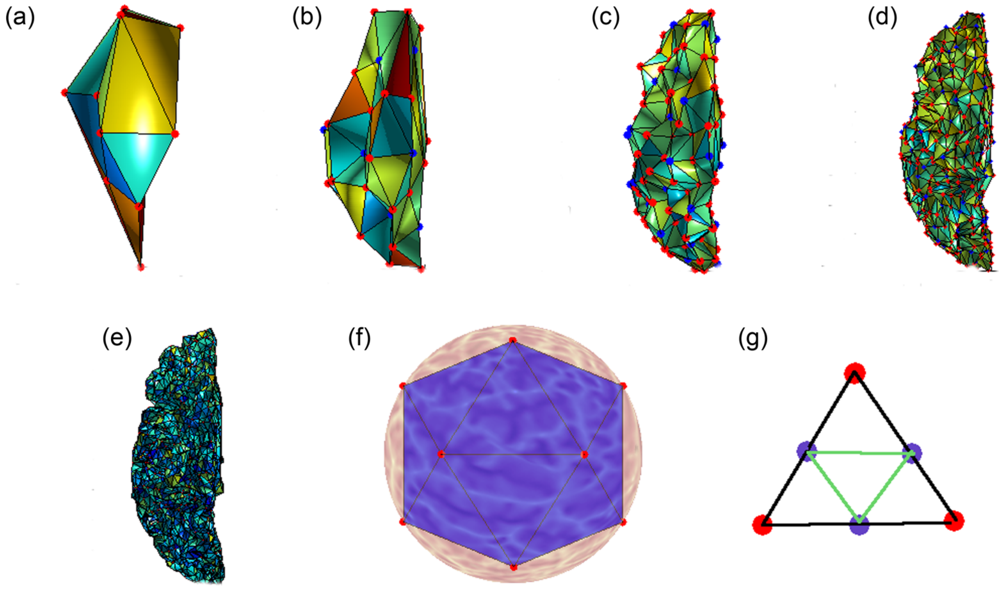

FIG. 1. (a)–(e) The renormalized lattices that represent a brain hemisphere used to solve the inverse problem at the different scales. (f) Each original lattice representing one hemisphere of the brain was inflated into a sphere [27]. Initially, for the coarsest lattice, an icosahedron was inscribed in the sphere. Regions of the sphere are identified with the icosahedron's face below. (g) The renormalization, in the inflated state is obtained by dividing each triangular face into four triangles. Deflation takes back to the lattice representations of the cortex. The dipoles possible positions at each scale are at the average centroid of all triangles in the original surface lying below the triangular faces derived through the renormalization procedure [(b)–(e)] or from the icosahedron faces (a).

observed in the scalp [15]. Such columnar structures have an apical size of 0.5 mm^2 [31], and given the area of the cortical mantle (1500 cm^2 [32,33]), a resolution higher than $O(10^5)$ sites violates physiological assumptions [15,34].

Starting at such continuum limit, consider the following general scenario. Sources $J(r_i,t)$, collectively denoted $\boldsymbol{J}$, with $r_i \in \Lambda_c$, give rise to signals $V_s(t)$ through a mechanism described by a Green's function operator G

$$V_s = G\boldsymbol{J}, \tag{1}$$

where for the EEG case we consider, V_s is the scalp potential. The Green's function G is a matrix that encodes the effect of the cortical dipole currents $\boldsymbol{J}$ responsible for the V_s array of scalp potentials at any (fixed) time. It is a reasonable approximation to consider the $\boldsymbol{J}$ as an array of scalars, since the direction of the dipole vector is supposed to be outward perpendicular to the cortex, due to its columnar organization discussed above. This linear model was used by Refs. [22] and has been discussed by Refs. [15,34–37], and [38].

To generate the artificial data we consider a particular set of time series $J(r_i,t)$ different from zero only at a few chosen positions. Not all the regions of the brain are active at the same time and only a few are relevant for a given task. This is the key to start thinking about dimensional reduction of the inverse problem. In this paper we consider up to five such positions. The forward problem is to obtain V_s from $\boldsymbol{J}$ at each time step. The inverse problem is to estimate $J(r_i,t)$ for all sites at Λ_D. In order to build Λ_D, we first inflate the original Λ_c to a sphere, while minimizing the pairwise distances [30]. An icosahedron is then inscribed into the sphere [Fig. 1(f)]. Regions of the sphere are identified with the icosahedron's face below. After dividing each face into four triangles, as indicated in Fig. 1(g), new regions in the sphere are assigned to the newly created plaquettes. This process is iterated five times until Λ_D has $2 \times 20 \times 4^5 \sim 4 \times 10^4$ [39]. Once the desired resolution is achieved, the vertices in the sphere can be reprojected back to the cortical space [Fig. 1(e)]. The average of the centroids of the plaquettes in the original Λ_c will define the position of each dipole used in the inverse problem. This is the lattice where most inverse problems are solved, and is the lattice where the VB, sLORETA, and MNE algorithms will be solved. The BRG-VB algorithm, however, consider all scales, from the icosahedron to the finest resolution desired [Figs. 1(a)–1(e)]. Each scale constitute a different Λ_d. The inverse problem will then be solved at each scale Λ_d, from the scalp electrode signals, which are only known at the electrode positions and include the addition of white zero-mean-independent Gaussian noise ξ

$$V = G\boldsymbol{J} + \xi = V_s + \xi. \tag{2}$$

The connectivity problem is to assess a causal model that represents the time interdependencies among the various recovered currents. To ensure transparency and reproducibility by other researchers, actual computations of the forward problem were performed using SPM software and FIELDTRIP toolbox [40], through a lead field matrix calculated using the realistic boundary element model (BEM) solutions based on the FreeSurfer MRI head template image within the SPM software containing G's definition used for $M = 128$ scalp electrodes placed according to the standard system.

Simulations employed different values of noise-to-signal ratio as imposed by

$$R_{\mathrm{NSR}} = \frac{\sigma_\xi^2}{\sigma_{V_s}^2}, \tag{3}$$

where σ_ξ^2 is the noise variance and $\sigma_{V_s}^2$ is the signal variance over all scalp sensors. The reason to use the expression in Eq. (3) rather than its inverse is its consistency with Sato *et al.* [22].

The forward problem, as stated, yields the potentials associated to a current distribution instantaneously. Dynamically varying currents result in time-dependent potentials. We can work with sources represented by independent time series or can add a causal structure to the sources' time series. By choosing to add a causal structure to the sources' times series, see Sec. IV, we simulate dependent time series. The challenge is then to identify conditions under which the causal structure can be recovered.

III. BRG FOR THE INVERSE PROBLEM

We used four different methods for the inverse problem. Since the backward renormalization group method is of recent introduction, it is briefly described next. For the VB and MNE, we used an in-house implementation and for sLoreta method, we used the implementation of Dalal *et al.* [23].

The application of Bayesian methods to inverse problems is now quite common. In our case the problem can be described as obtaining an approximation to the ground state of a Hamiltonian with both ferromagnetic and antiferromagnetic interactions. This is done by iteration of the variational Bayes algorithm, which can be described as an iterative mean-field method. It clearly is very useful to start from a good initial approximation. A good candidate for the initial approximation is obtained from the solution of the problem first on a coarser scale. A second iterative process works on successive finer representations of the lattices.

The BRG-VB method works by extracting information from the posterior in a way similar to the variational Bayes approach of Ref. [22], with the extra ingredient that it employs RG ideas as described in Refs. [26,28,29] to systematically generate informative prior distributions from the posteriors obtained by solving the problem at a coarse-grain representation of the cortex. The RG is sometimes referred to as a semigroup since it can not be inverted. This is true for the configurations of the degrees of freedom, but in the space of coupling constants (hyperparameters) the RG map can be inverted and from a coarse-grain distribution, the distribution on a more refined lattice can be obtained.

Consider the problem defined at a given resolution d, i.e., a lattice Λ_d of N_d sites r_i^d is used to represent the cortex where the dipoles live (see Fig. 1). In Eq. (2), the dimensions of the different variables arrays are as follows. If there are M sensors and T time measurements, then the matrices $V, \boldsymbol{J}_d, G_d$, and ξ are of dimensions $M \times T$, $N_d \times T$, $N_d \times M$, and $M \times T$, respectively. We now consider a particular time step and the process will be repeated for every time step. To do inference we need to discuss priors, likelihoods, and any informational constraints. The model for the dipole density prior probability density $Q_0(\boldsymbol{J}_d) = \prod_i Q(J_i^d|\alpha_i^d)$ is parametrized by a set of unknown precision parameters $\boldsymbol{\alpha}_d = \{\alpha_i^d\}$. Given $\boldsymbol{\alpha}_d$ the J_i^d's are mutually independent and the joint prior will be a product over sites. We now describe how to proceed at a particular site $i \in \Lambda_d$. Each α_i^d is the inverse of the variance of the zero mean Gaussian prior for the dipole density amplitude J_i^d. Hyperpriors for each individual member of α_i^d are needed since these are unknown. Sato *et al.* [22] use a product of Γ hyperprior distributions $\prod_i \Gamma(\alpha_i^d|\hat{\alpha}_i^d,\hat{\gamma}_i^d)$. Integrating over the values of α_i^d with the Gaussian priors, the Γ leads to Student's t distributions for J_i^d. At each site r_i^d of the cortex, the prior density is given by

$$Q_0\big(J_i^d\big|\hat{\alpha}_i^d,\gamma_i^d\big) = \int_0^\infty \frac{\alpha^{1/2}}{\sqrt{2\pi}} e^{-\frac{\alpha(J_i^d)^2}{2}}\Gamma\big(\alpha\big|\hat{\alpha}_i^d,\hat{\gamma}_i^d\big)d\alpha$$
$$= \sqrt{\frac{\hat{\alpha}_i^d}{2\pi\gamma_i^d}}\frac{\Gamma\big(\gamma_i^d+\frac{1}{2}\big)}{\Gamma(\gamma_i^d)}\frac{1}{\big[1+\frac{(J_i^d)^2\hat{\alpha}_i^d}{2\gamma_i^d}\big]^{\gamma_i^d+1/2}}, \tag{4}$$

however, the posterior will not necessarily be in the same Student t family. A projection using the variational Bayes method, leads back to the Student t family generating a dynamics of the hyperparameters of the Γ's, that converges to a final value at that unique scale. Their method can be succinctly described by the iterative mapping from the hyperparameters of the prior to those of the posterior

$$\big(\hat{\boldsymbol{\alpha}}_d^0,\boldsymbol{\gamma}_d^0\big) \xrightarrow{\text{variational Bayes}} \big(\hat{\boldsymbol{\alpha}}_d^f,\boldsymbol{\gamma}_d^f\big). \tag{5}$$

In Sato *et al.* [22] the prior of the dipole density was taken as spatially constant, meaning that the initial conditions are the same for every site. It turns out to be preferable to use priors that are not constant over space, but which carry information obtained from solving the problem at a coarser scale. This means that the prior values of the hyperparameters can depend on the lattice site. In order to do this, Caticha [26], following multiscale ideas in da Rocha Amaral *et al.* [28,29], considered a maximum entropy problem where the relevant space is formed by the dipole variables at the two scales and the electrode potentials. Thus, we seek the maximization of the relative entropy

$$S[P||Q] = -\int P(\boldsymbol{J}_d,\boldsymbol{J}_{d-1},v)$$
$$\times \ln\frac{P(\boldsymbol{J}_d,\boldsymbol{J}_{d-1},v)}{Q(\boldsymbol{J}_d,\boldsymbol{J}_{d-1},v)}d\boldsymbol{J}_d d\boldsymbol{J}_{d-1}dv \tag{6}$$

to obtain $P(\boldsymbol{J}_d,\boldsymbol{J}_{d-1},v)$ from a prior $Q(\boldsymbol{J}_d,\boldsymbol{J}_{d-1},v)$. The idea behind this is that we have incomplete information about the currents at the two resolutions and also about the potential v. The distribution P that maximizes $S[P||Q]$ is subject to the constraints of what we know. In addition to normalization, $P(\boldsymbol{J}_d,\boldsymbol{J}_{d-1},v)$ is subject to the following constraints.

(i) Integrating over all configurations of the dipole variables at scale $d-1$ and d yields the marginal v distribution, constrained to $P(v) = \delta(v-V)$, where by v is the variable that represents the potential and V is the array of measured data.

(ii) The marginal $Q(\boldsymbol{J}_{d-1})$ is given, e.g., by the Student t-distribution product family.

(iii) Knowledge about the relation between the dipole representation at different scales coded by $Q(\boldsymbol{J}_d|\boldsymbol{J}_{d-1})$ is obtained from the renormalization transformation.

(iv) Given $\boldsymbol{J}_d$, knowledge of $\boldsymbol{J}_{d-1}$ is irrelevant for v: $Q(v|\boldsymbol{J}_d\boldsymbol{J}_{d-1}) = Q(v|\boldsymbol{J}_d)$. This states simply that for the forward problem, when the finer scale information of the currents is available, the value of coarser scale renormalized variables brings no new information.

Marginalization and the product rule of probability give

$$Q(\boldsymbol{J}_d) = \int Q(\boldsymbol{J}_{d-1})Q(\boldsymbol{J}_d|\boldsymbol{J}_{d-1})d\boldsymbol{J}_{d-1}, \tag{7}$$

which can be calculated from (ii) and (iii). Solving the maximization problem leads to the maximum entropy distribution $P(\boldsymbol{J}_d,\boldsymbol{J}_{d-1},v)$. The important result is that the fine-grained marginal $P(\boldsymbol{J}_d) = \int P(\boldsymbol{J}_d,\boldsymbol{J}_{d-1},v)d\boldsymbol{J}_{d-1}dv$, is given by (see Appendix A)

$$P(\boldsymbol{J}_d) = Q(\boldsymbol{J}_d|V) = \frac{Q(\boldsymbol{J}_d)Q(V|\boldsymbol{J}_d)}{Q(V)}, \tag{8}$$

where instead of the variable v, the actual value of the measured potentials V appears. Inference using maximum entropy gives the same result as Bayes posterior rule when starting from the same prior uses constraints imposed by data measurements [41]. This is almost what one would have expected, Bayes theorem but with a twist: that the prior at this new scale [Eq. (7)] is obtained by whatever information is available from $\boldsymbol{J}_{d-1}$, i.e., $Q(\boldsymbol{J}_{d-1})$ and the backward renormalization procedure $Q(\boldsymbol{J}_d|\boldsymbol{J}_{d-1})$. Of course the best that can be done for $Q(\boldsymbol{J}_{d-1})$ is to use the result obtained at the previous scale, the coarse posterior.

Restricting the distributions to Student's t-distribution products, we have to use $Q(\boldsymbol{J}_d|\hat{\boldsymbol{\alpha}}_d^0,\gamma_d^0)$, from Eq. (7) given by

$$Q\big(\boldsymbol{J}_d\big|\hat{\boldsymbol{\alpha}}_d^0,\boldsymbol{\gamma}_d^0\big) \approx \int Q\big(\boldsymbol{J}_{d-1}\big|\hat{\boldsymbol{\alpha}}_{d-1}^f,\boldsymbol{\gamma}_{d-1}^f\big)Q(\boldsymbol{J}_d|\boldsymbol{J}_{d-1})d\boldsymbol{J}_{d-1}. \tag{9}$$

The posterior in the coarser scale $d-1$, coded by $(\hat{\boldsymbol{\alpha}}_{d-1}^f,\boldsymbol{\gamma}_{d-1}^f)$ induces a prior in the d scale parametrized by $(\hat{\boldsymbol{\alpha}}_d^0,\boldsymbol{\gamma}_d^0)$. We start at the coarsest resolution with the same (α_0^i,γ_0^i) initial values at every site of the coarsest lattice Λ_0. Next obtain via variational Bayes the parameters for the posterior of $\boldsymbol{J}_0$ from Eq. (5) and proceed for the next scales as represented by the map:

$$\big(\hat{\boldsymbol{\alpha}}_{d-1}^f,\boldsymbol{\gamma}_{d-1}^f\big) \xrightarrow{\text{BackRenorm}} \big(\hat{\boldsymbol{\alpha}}_d^0,\boldsymbol{\gamma}_d^0\big). \tag{10}$$

Beginning with a uniform prior at the coarsest scale, that is a set of parameters $(\hat{\boldsymbol{\alpha}}_0^0,\boldsymbol{\gamma}_0^0)$ uniform over the lattice Λ_0, we iterate the mapping

$$\big(\hat{\boldsymbol{\alpha}}_0^0,\boldsymbol{\gamma}_0^0\big) \overset{\text{VB}}{\to} \dots \overset{\text{BackRenorm}}{\to} \big(\hat{\boldsymbol{\alpha}}_d^0,\boldsymbol{\gamma}_d^0\big) \overset{\text{VB}}{\to} \big(\hat{\boldsymbol{\alpha}}_d^f,\boldsymbol{\gamma}_d^f\big)$$
$$\xrightarrow{\text{BackRenorm}} \big(\hat{\boldsymbol{\alpha}}_{d+1}^0,\boldsymbol{\gamma}_{d+1}^0\big) \overset{\text{VB}}{\to} \dots \tag{11}$$

to finally obtain a posterior at the finest scales described by $(\hat{\boldsymbol{\alpha}}_D^f,\boldsymbol{\gamma}_D^f)$, the desired answer to the inference problem since they give an answer to the query about active regions.

This mapping from the coarse posterior to the finer prior can only be implemented in an approximate way. There is the additional problem that due to the convoluted shape of the cortex: dipole directions on different scales do not coincide. Also the spatial part of renormalization step is quite messy. A simple model of the renormalization, see the Appendix B, suggests $(\hat{\boldsymbol{\alpha}}^0_d,\boldsymbol{\gamma}^0_d) \approx (\hat{\boldsymbol{\alpha}}^f_{d-1},\boldsymbol{\gamma}^f_{d-1})$ as an approximation. However, we have used the prior hyperparameter at position i of lattice Λ_d given by

$$\frac{1}{\hat{\alpha}^0_{i,d}} = \frac{1}{\hat{\alpha}^f_{I,d-1}} + \frac{1}{3}\sum_{n.n}\frac{1}{\hat{\alpha}^f_{I_{nn},d-1}} + \frac{1}{9}\sum_{n.n.n}\frac{1}{\hat{\alpha}^f_{I_{\rm nnn},d-1}}, \qquad (12)$$

since, numerically, it was found that bringing information from nearest- ($I_{\rm nn}$) and next-nearest neighbor ($I_{\rm nnn}$) faces increased the quality of the inference. Since adding the neighboring terms increases the prior uncertainty about $J_{i,d}$, this can be seen as a conservative choice of the new prior. For simplicity we also hold $\gamma^0_{i,d}$. While such a simple prescription may be improved we make two comments. First, that we only need an approximation to the parameters at the higher resolution since they will be improved by the variational Bayes refinement. Second, and theoretically very important, the reuse of data at different coarseness levels might seem to be a reuse of the data in a simple Bayesian approach, which is not the case in entropic inference, since imposing an already satisfied constraint will not lead to a posterior different from the prior.

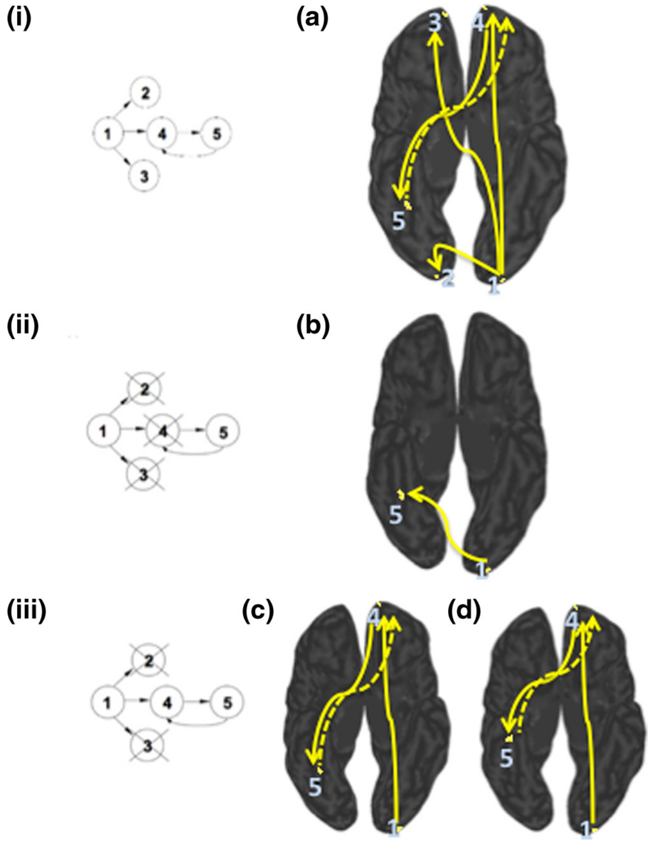

FIG. 2. The simulated scenarios. All use identical time series structures. In the different scenarios the number of electrically active time series that represent dipole currents are: (a) with five ($q_{1-5} = 1$), (b) with two ($q_{1,5} = 1, q_{2,3,4} = 0$), and (c) and (d) with three ($q_{1,4,5} = 1, q_{2,3} = 0$). Crossed out nodes have $q_a = 0$, uncrossed nodes $q_a = 1$. Scenarios (c) and (d) differ only by the position of the sources. The actual values used to generate the time series of system 13 were: $a_{11} = .95, a_{12} = 0.9025, a_{21} = .5, a_{31} - .4, a_{41} = -.5, a_{42} = \sqrt{2}/4, a_{43} = \sqrt{2}/4, a_{51} = -\sqrt{2}/4, a_{52} = \sqrt{2}/4$.

IV. CONNECTIVITY

A. Model for the dipole source dynamics generation

The above method is applicable instantaneously: given the dipole currents at time n the hyperparameters can be obtained. However, if the currents are time dependent, then the hyperparameters will inherit a time dependence. We consider the following model for the time dependence of the set of time series $\{x_a(n)\}$, which are located at a few sites in lattice Λ_c. We choose to generate five causally related time series. Each series is associated to an active region. However, despite being causally active a source may or may not be electrically active. This is indicated by a time-independent variable q_a, which takes value one if the source is electrically active and zero if not. The dipole current source that feeds the forward model is given by $J_a(n) = q_a x_a(n)$. The choice of the set of $\{q_a\}$ determines what is called a scenario. The scenarios we simulate are shown in Fig. 2. The uncrossed units are electrically active $q_a = 1$ and the crossed out units are electrically inactive $q_a = 0$. The underlying dynamics between source signals was imposed using a multivariate autoregressive (MAR) model involving five dynamic variables drawn from Example 5 in Ref. [2] (Fig. 2):

$$\begin{aligned} x_1(n) &= a_{11}x_1(n-1) - a_{12}x_1(n-2) + \omega_1(n)\\ x_2(n) &= a_{21}x_1(n-2) + \omega_2(n)\\ x_3(n) &= -a_{31}x_1(n-3) + \omega_3(n)\\ x_4(n) &= -a_{41}x_1(n-2) + a_{42}x_2(n-1)\\ &\quad + a_{43}x_3(n-2) + \omega_4(n)\\ x_5(n) &= -a_{51}x_4(n-1) + a_{52}x_5(n-1) + \omega_5(n), \qquad (13)\end{aligned}$$

where the a_{bc}'s are non-negative constants and describe the contribution of x_a at a certain time to the value of x_b at a later time. The ω_a are independent Gaussian noise processes with zero mean and unit variance. The signal from the source x_1 goes to x_2, x_3, and x_4 directly but only reaches x_5 indirectly via x_4. The illustrative computations shown here employed $T = 400$ simulated time series sample points for 100 performed simulations. The dynamics in model 13 has been widely used by many researchers for benchmarking purposes [42], where the choice of a_{bc} coefficients was chosen to ensure that oscillations generated at $x_1(n)$ propagate to other structures. The specific values are shown in Fig. 2.

We performed systematic investigation of impairments due to noise corrupting the electrode potentials for the five-dipole scenario [Fig. 2(a)] using the noise-to-signal ratios $R_{\rm NSR}$ of 0.25, 0.1, 0.01, and 0.001 (the practically noiseless condition) and for the two-dipole scenario [Fig. 2(b)] using $R_{\rm NSR}$s of 0.01, 0.1, and 0.25. For the tree-dipole scenarios [Figs. 2(c) and 2(d)], only the value of $R_{\rm NSR} = 0.1$, as adopted by Sato *et al.* [22], was used.

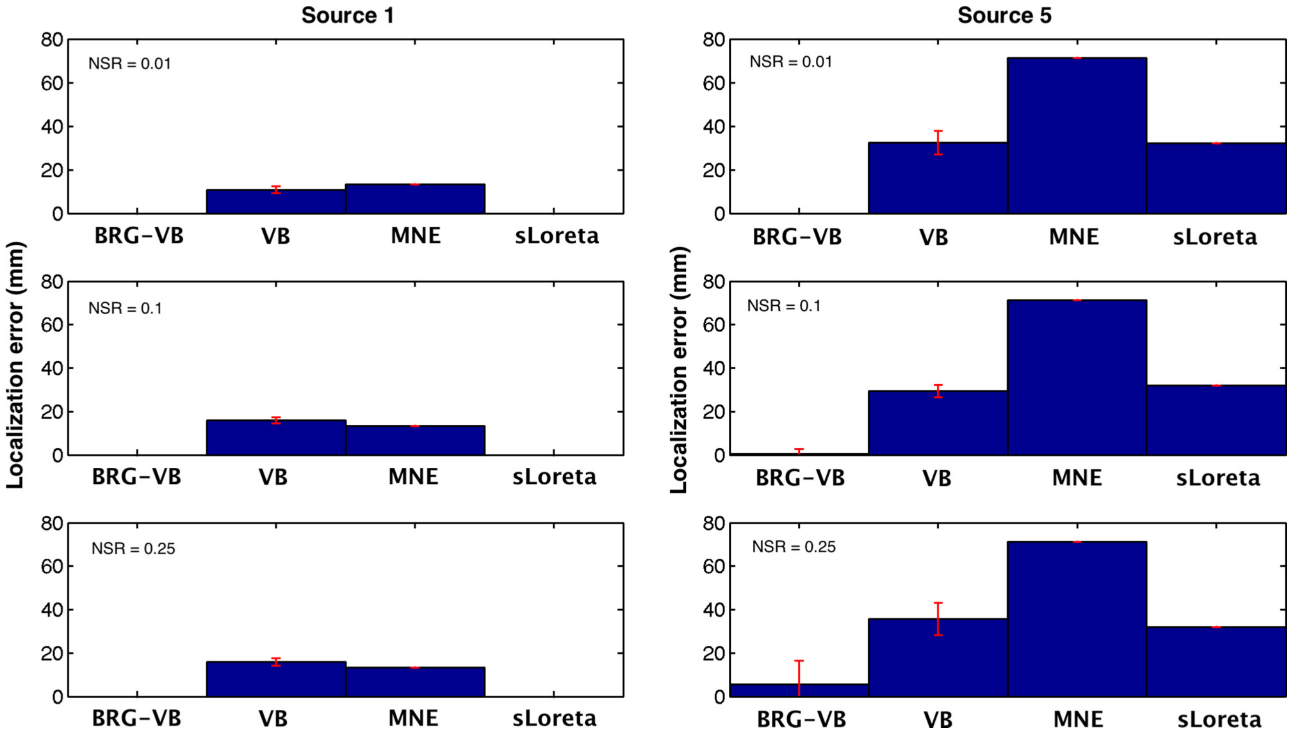

FIG. 3. Localization error for different noise levels ($R_{\mathrm{NSR}} = 0.01$, 0.1, and 0.25) for two-dipole scenario [Fig. 2(b)]. Error measured in mm. Note that source 5 is deeper than source 1 and its localization is harder. Only BRG-VB finds both sources with small error. sLoreta finds source 1 with a small error but it increases for source 5. VB and MNE are equivalent on source 1 but VB is better for source 5 while MNE is more affected by the depth of source 5. Error bars are standard deviations obtained from 100 simulations.

B. Connectivity inference

Partial directed coherence (PDC) was chosen as the connectivity benchmark criterion because it is a frequency domain quantifier of the concept of Granger causality [19] (see Appendix C for details) and because frequency domain representations have important physiological correlates in EEG such as sleep stages [20].

PDC interaction from a source structure at position j towards another structure at position i is given by

$$\pi_{ij}(\nu) = \frac{\bar{A}_{ij}(\nu)}{\sqrt{\sum_{k=1}^{N} \bar{A}_{ki}(\nu)\bar{A}^{*}_{kj}(\nu)}}, \tag{14}$$

for some normalized frequency ν between 0 and 0.5 where $\bar{A}_{ij}(\nu)$ are the elements of the matrix $\bar{\mathbf{A}}(\nu)$ given by

$$\bar{\mathbf{A}}(\nu) = \mathbf{I} - \sum_{r=1}^{p} \mathbf{A}_r z^{-r}\big|_{z=e^{-j2\pi\nu}}, \tag{15}$$

where $\mathbf{I}$ is the identity matrix and $\mathbf{A}_r$ are obtained from the adjustment of a multichannel autoregressive model of the form:

$$\boldsymbol{J}(n) = \sum_{r=1}^{p} \mathbf{A}_r \boldsymbol{J}(n-r) + \boldsymbol{\omega}(n), \tag{16}$$

where $\boldsymbol{J}(n) = [J_1(n), \ldots, J_N(n)]^T$ is the array of sources and $\boldsymbol{\omega}(n)$ is a zero mean vector white Gaussian noise process

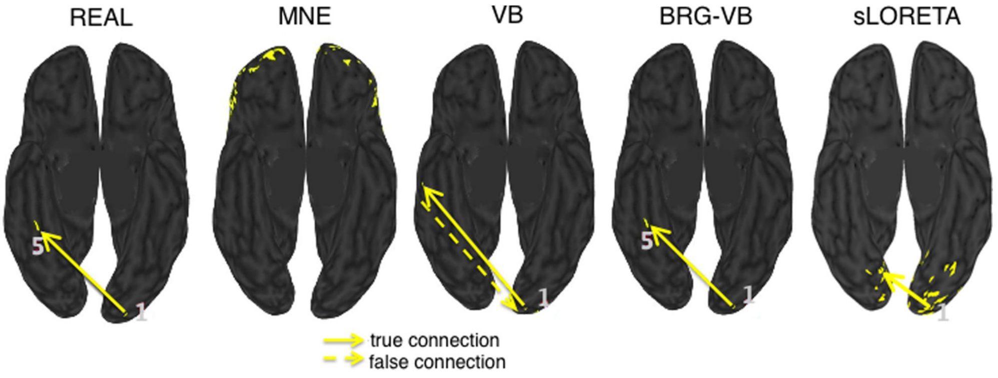

FIG. 4. For two-dipole scenario [Fig. 2(b)] the simulated dipole cortical surface positions and the estimated currents using MNE, sLoreta, VB, and BRG-VB are contrasted. $R_{\mathrm{NSR}} = 0.1$ independent Gaussian noise was added to scalp electrodes. The arrows represent the estimated (PDC above 0.1) and simulated connections between sources (points in yellow).

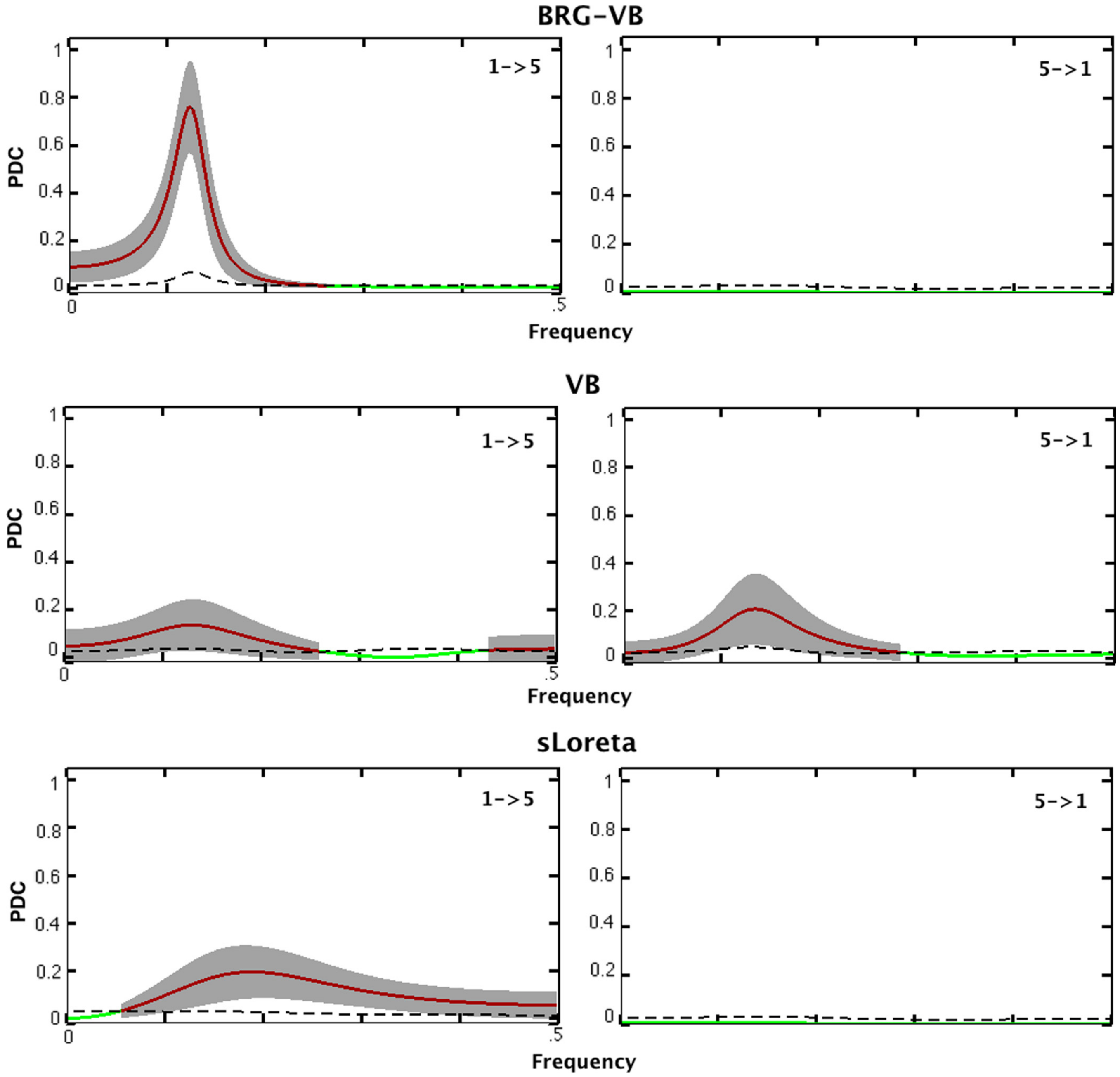

FIG. 5. Two dipole scenario with sources 1 and 5 defined in Fig. 2(b). PDC connectivity reconstructed by the BRG-VB, VB, and sLoreta methods for noise level of $R_{\mathrm{NSR}} = 0.1$. Left: forward connection from 1 to 5, right: feedback connection from 5 to 1. Dark red solid lines indicate significant PDC (red) and turn into green nonsignificant lines (green) as they fall below the dashed dark lines that represent the null connectivity hypothesis threshold level of $\alpha = 0.05$ significance level. Gray shadows represent the confidence intervals [43].

[44]. Following determination of each source, we selected the time series of highest power within its ROI to subject it to connectivity appraisal via PDC.

V. RESULTS

We first did a systematic comparison between the different algorithms used in the inverse problem. While this is of interest in itself, we feel that details are beyond the scope of this paper. We only present a summary of the source localization results. Consistently, throughout the different scenarios, the backward RG gave better results than the other methods. It is an obvious fact that the localization of sources is simpler when fewer sources are active and we begin by analyzing the simplest case. As an example, we show in Fig. 3 the localization errors associated with the source reconstruction from the two active source scenario of Fig. 2(b). In this scenario source number 1 is near the scalp and source number 5 is deep into the cortex. Due to the decay of the Green's function, noise affects much more the localization of deep sources and this

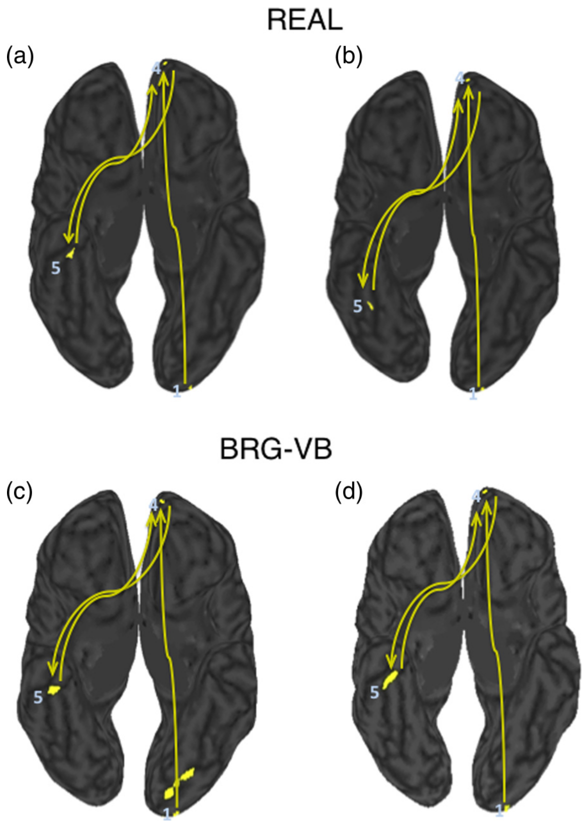

FIG. 6. Top (a) and (b): Original positions for two three-dipole scenarios [Figs. 2(c) and 2(d), respectively] with arrows representing the simulated connections. Bottom (c) and (d): The corresponding BRG-VB result overlaid onto the cortical surface at a representative time point with arrows representing the estimated connections ($\text{PDC} > 0.1$) across sources. $R_{\text{NSR}} = 0.1$ independent Gaussian noise was added to scalp electrodes' potentials.

is reflected in the larger error observed for source 5. We now look for the connectivity inference using PDC. Still for the two source scenario, results are shown in Fig. 4. PDC working with the localization data of BRG-VB estimates correctly the causal relations. MNE does not find any significant causal relation, pure VB sources lead to symmetric causal influence and sLoreta finds a seemingly correct causal effect at the cost of localization errors. The connectivity indication shown in Fig. 4 is obtained from the position of the sources and from the results shown in Fig. 5 where the PDC estimate as a function of frequency [see Eq. (14)] is shown. MNE is not shown because it did not go above the significance level for any frequency. Figure 5 shows BRG-VB's superior performance, which confirms the corresponding estimated connectivity from 1 to 5 (Fig. 5 top) for $R_{\text{NSR}} = 0.1$. Note that in Fig. 5 bottom, the sLoreta method finds a weak connection (from 1 to 5), which is, however, at the wrong position (away from the first and second neighbors) for source 5 and the VB method found sources 1 and 5 at wrong cortical positions (away from the first and second neighbors) and consequently, Fig. 5 (middle) shows a nonexistent backward connection from 5 to 1 and a weak true forward connection from 1 to 5. Note that the PDC connectivity graphs portray confidence intervals and the null hypothesis threshold.

Turning on the activity of dipole 4 to simulate the three-dipole scenarios [Figs. 2(c) and 2(d)] increases greatly the difficulty of the inverse problem and we could not get satisfactory source identification for MNE, VB, nor sLoreta, hence only the causality results for BRG-VB sources will be discussed.

The BRG-VB reconstructions are shown in Fig. 6, which are obtained from the corresponding estimated PDC connectivities using $R_{\text{NSR}} = 0.1$ (Fig. 7). Correct dipole 5 reconstruction was only obtained in Fig. 6(c). Figure 7(a) also presents the connectivity plot using the original position for source 5, indicating possible signal impairment. The connectivity plots [Figs. 7(a) and 7(b)] differ somewhat in magnitude for connection from 4 to 5.

Now we concentrate on the five-dipole scenario [Fig. 2(a)] to gauge BRG-VB reconstruction sensitivity as a function of added electrode noise level. The PDC connections are shown in Fig. 9. The corresponding estimated PDC change as a function of sensor noise level can be viewed in Fig. 8 with wrong feedback connections (from 3 to 1, from 3 to 2, from 4 to 3, and from 4 to 1) being observed only at higher noise levels [Figs. 8(c) and 8(d)]. Significant PDC was only larger than 0.1 for 4 to 3 connection. Even though BRG-VB managed to detect active faces on the cortical surface close to the artificially imposed ones at all noise levels, the locally reconstructed signal became degraded to the point of clearly hindering adequate connectivity inference. This is better illustrated in Fig. 10, where we showed the percentage of significant PDC values as a function of noise level on 100 simulated trials.

VI. DISCUSSION

We first address the inverse problem. The BRG method works by dividing the inference problem into several steps, it is based on the intuition that solving the related problem at a coarser resolution should be of interest at the finer resolution. If this is true then it can be of importance in many inverse problems. Trying to identify candidates where it can be useful poses a question about the main ingredients necessary for the backward renormalization to be of any help in the inferential process. To do this we have to identify what new information was brought in by this method. At this point it seems that inference problems where there is a spatial structure that can be represented at different resolutions levels are the candidates for applications. The identification of sources is hindered by noise levels and the effective noise level at the coarser scale is expected to decrease by $1/\sqrt{n}$ with respect to the noise level of the finer scale, where n (=4) is the ratio of the number of degrees of freedom in the two representations. This certainly deserves more theoretical and practical studies.

Now we discuss the causal influence part of our work. We ranked connectivity inference via PDC performance under a representative set of source reconstruction methods. The BRG-VB method was more robust under the tested artificial scenarios involving distinct source positions within the cortical surface and under different sensor noise impairment levels. The popular techniques VB, MNE and sLoreta were not able to reconstruct the sources correctly for the simplest scenario of connected two-dipoles. The sLoreta technique finds a weaker connection at the wrong position and VB

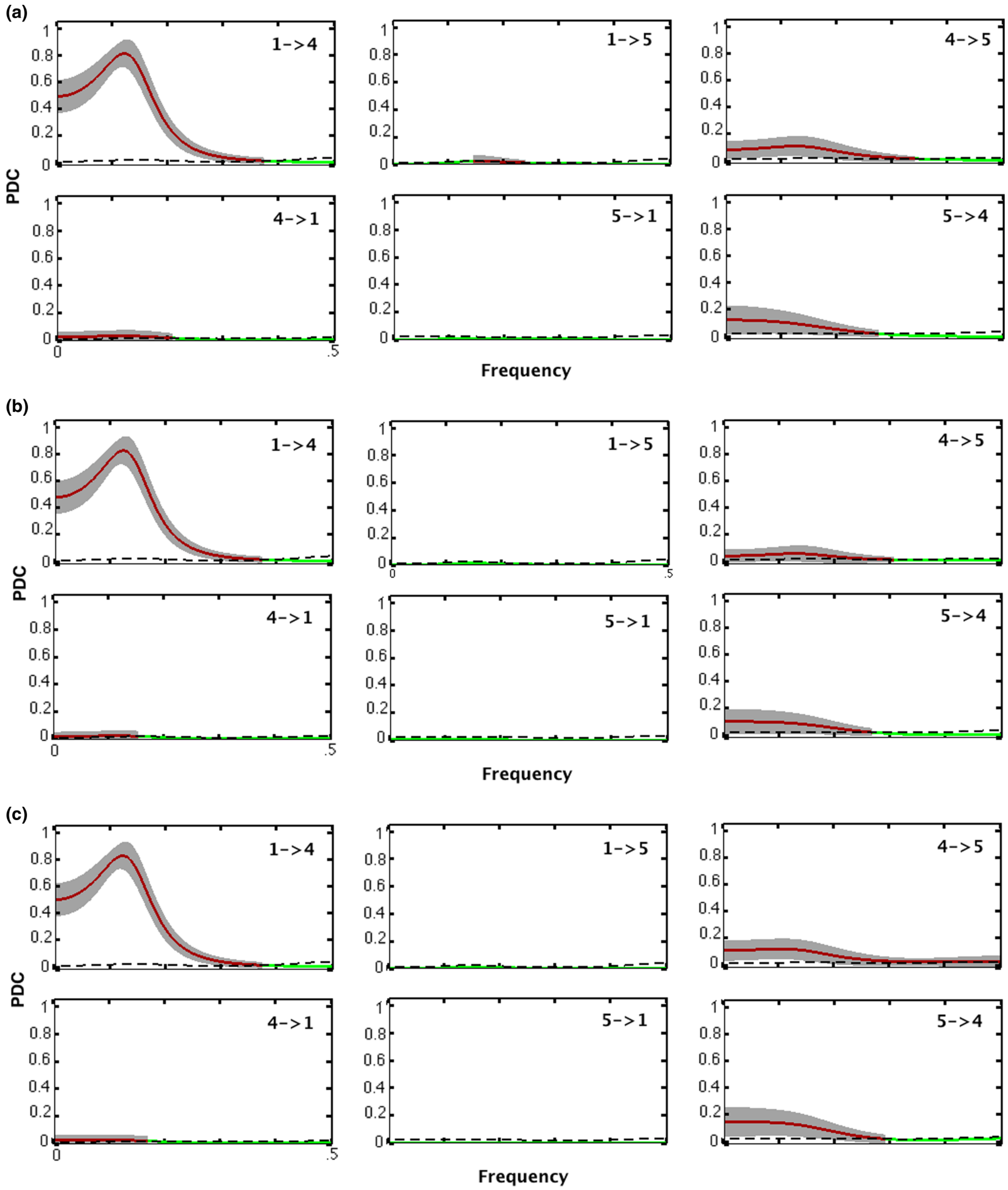

FIG. 7. Connectivity plots between sources reconstructed using BRG-VB for the two three-dipole scenarios in Figs. 2(c) and 2(d). Top: Connectivity plots of Fig. 6(d) using both estimated signal and position for source 1 (reconstructed correctly) and (a) using the original source 5 position and (b) its estimated position (reconstructed at a wrong position). Bottom (c): Connectivity corresponding to Fig. 6(c) with its correctly reconstructed source positions for $R_{\mathrm{NSR}} = 0.1$ for plot conventions as in Fig. 5.

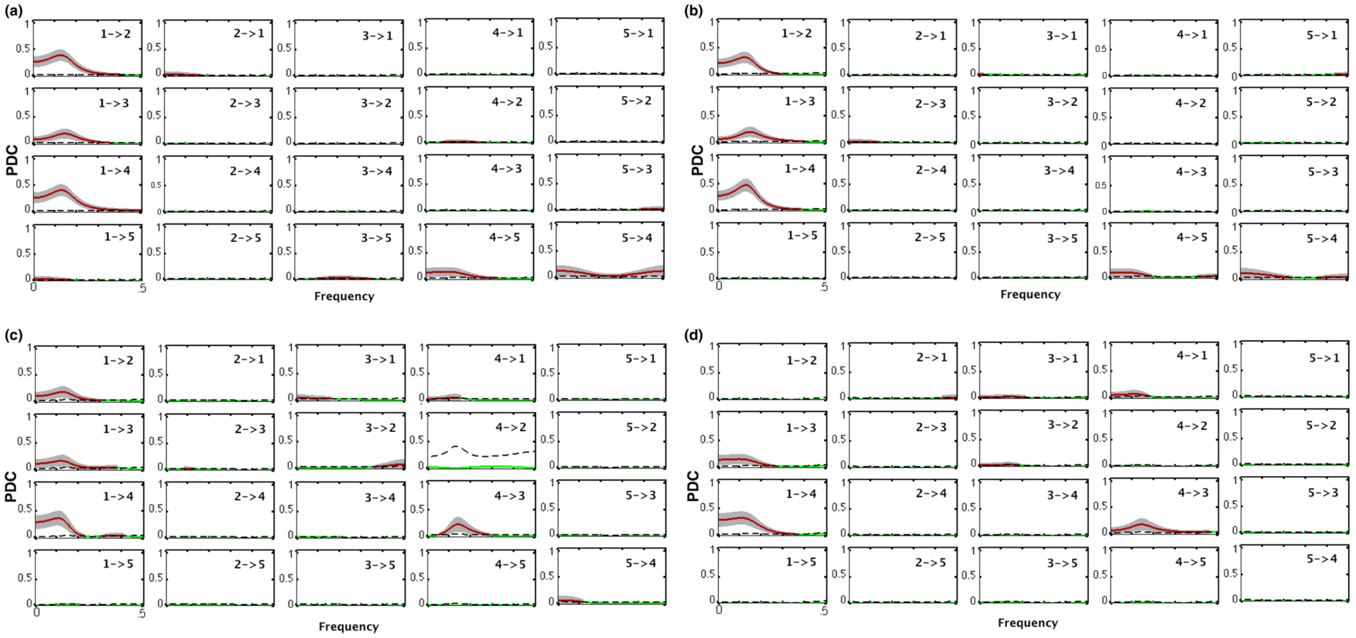

FIG. 8. Connectivity plots on sources estimated by the BRG-VB for artificial data with five interconnected dipoles corrupted with (a) practically noiseless ($R_{\mathrm{NSR}} = 0.001$); (b) $R_{\mathrm{NSR}} = 0.01$; (c) $R_{\mathrm{NSR}} = 0.1$; and (d) $R_{\mathrm{NSR}} = 0.25$. Lines are as described in Fig. 5.

identifies a nonexisting backward connection from 5 to 1. Most importantly, our results showed that (i) the inverse problem solution does not affect the direction of the flow of information when the dipole sources are found correctly and (ii) even though BRG-VB managed to detect active faces on the cortical surface close to the imposed ones at all noise levels, when excessive noise was present the locally reconstructed signal became degraded to the point of clearly hindering adequate connectivity inference. Furthermore, the source position affected the reconstruction indicating that the cortical surface geometry impacts localization accuracy. This confirms previous studies that showed that both the forward model and the spatial resolution are crucial for correct reconstruction [45–48].

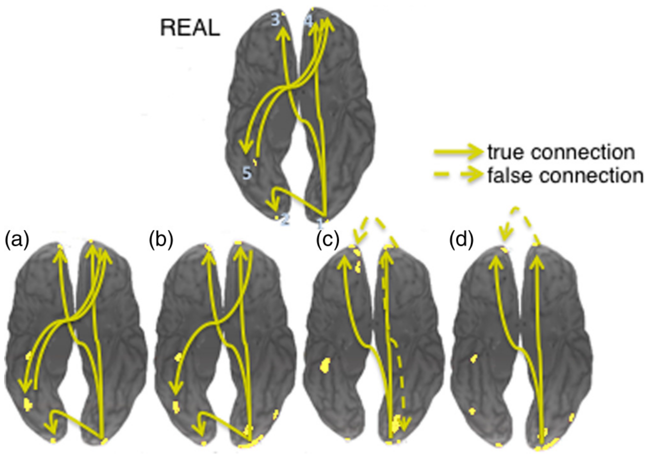

FIG. 9. Top: Original positions for the five-dipole scenario [Fig. 2(a)]. Arrows represent the simulated connections across sources. Bottom: BRG-VB reconstruction results under increasing noise levels (a) practically noiseless ($R_{\mathrm{NSR}} = 0.001$), (b) $R_{\mathrm{NSR}} = 0.01$, (c) $R_{\mathrm{NSR}} = 0.1$, and (d) $R_{\mathrm{NSR}} = 0.25$. Reconstructed sources (in red) were overlaid onto the cortical surface at a representative sample point, where the estimated current is maximum at that point. Arrows represent the estimated connections across sources with significant PDC above 0.2.

Here, we have performed a systematic simulation to examine the impact of interconnected sources on inverse problem solutions in the EEG context. An interesting study, in the MEG context, has been performed by Sekihara *et al.* [49], in which they investigated MEG adaptive beam-former techniques under the effects of two significantly correlated sources observing major inferred signal-intensity reductions and distortions in the estimated time signals.

Some works [47,49] have examined source reconstruction methods for deep source localization whose adequate attainment has proved challenging. This has been observed in our results, when sources were simulated at the temporal lobe (here represented by source 5). The use of multimodal information [50,51], combining fMRI-EEG-MEG data has been suggested as an alternative that needs to be examined via the present systematic methodology.

The present paper confirms the feasibility of accurate connectivity analysis based on reducing the dimensionality of the problem to the dipole source space provided that an accurate ROI determination algorithm is used under favorable NSR conditions. This conclusion calls for further research given the observed potentially deleterious effect of dipole placement and the amount of added noise. The use of more realistic artificial data with distributed source and existence of correlated noise must also be investigated. A research program to probe further into these effects in the BRG-VB context is a topic for future research.

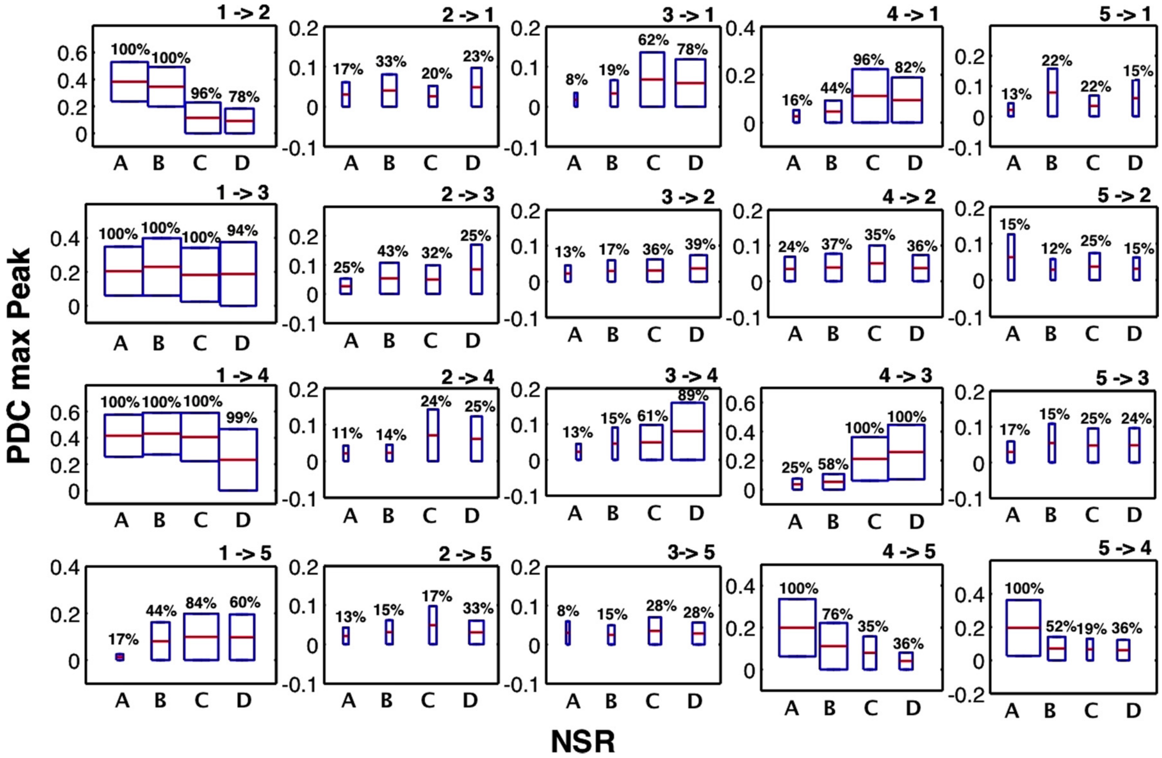

FIG. 10. Significant PDC maximum peak as a function of added electrode noise level (NSR) for sources estimated by the BRG-VB for the five-dipole scenario. The x axis represents (a) $R_{\mathrm{NSR}} = 0.001$; (b)$R_{\mathrm{NSR}} = 0.01$; (c)$R_{\mathrm{NSR}} = 0.1$; and (d)$R_{\mathrm{NSR}} = 0.25$. The plotted boxes indicate the minimum and maximum significant PDC for 100 simulated trials. The percentage on each box indicates the portion of significant PDC values for all trials for each NSR.

ACKNOWLEDGMENTS

The authors would like to thank K. Sameshima for valuable discussions. This work had financial support from FAPESP and CNPq/MCTI-FAPEG. CNPq Grant No. 307163/2013-0 to L.A.B. is also gratefully acknowledged. L.S.B acknowledges a CAPES fellowship and N.C. received support from CNAIPS-USP.

APPENDIX A: MAXIMIZATION OF THE ENTROPY

The variational problem is to obtain the maximum argument of

$$\begin{aligned} &S[P||Q]\\ &= -\int P(J_d,J_{d-1},V)\ln\frac{P(J_d,J_{d-1},V)}{Q(J_d,J_{d-1},V)}\\ &+\int\lambda(V)\bigg(\int P(J_d,J_{d-1},V)dJ_dJ_{d-1}-\delta(V-v')\bigg)dV\\ &+\lambda_0\bigg(\int P(J_d,J_{d-1},V)dJ_dJ_{d-1}dV-1\bigg)\\ &\times dJ_d dJ_{d-1}dV \end{aligned} \tag{A1}$$

when the information comes in form of data and we follow the result in Ref. [41]. Note that there is a Lagrange multiplier for each value of V. Not all constraints come in the form of expected values. The fact that $P(V) = \delta(V - v')$ means that the variations are not general but only $P(J_d, J_{d-1}|V)$ can be varied. The advantage of Lagrange multipliers is that we can go ahead without worrying and then impose the constraints. The solution is

$$P(J_d,J_{d-1},V) = Q(J_d,J_{d-1},V)\frac{e^{\lambda(V)}}{Z} \tag{A2}$$

for an appropriate normalization Z. The set of Lagrange multipliers is obtained by imposing the constraints, such that the marginal posterior of V is given by

$$\int P(J_d,J_{d-1},V)dJ_dJ_{d-1} = \int Q(J_d,J_{d-1},V)\frac{e^{\lambda(V)}}{Z}dJ_dJ_{d-1}. \tag{A3}$$

It follows that

$$\frac{e^{\lambda(V)}}{Z} = \frac{\delta(V-v')}{Q(V)} \tag{A4}$$

and the joint posterior

$$P(J_d,J_{d-1},V) = Q(J_d,J_{d-1},V)\frac{\delta(V-v')}{Q(V)}. \tag{A5}$$

Marginalizing with respect to V gives

$$P(J_d,J_{d-1}) = \frac{Q(J_d,J_{d-1},v')}{Q(v')} = Q(J_d,J_{d-1}|v') \tag{A6}$$

and further marginalization over J_{d-1} gives

$$P(J_d) = \frac{Q(J_d,v')}{Q(v')} = Q(J_d|v') = Q(J_d)\frac{Q(v'|J_d)}{Q(v')}. \tag{A7}$$

This is just the expression of Bayes theorem. This is a deep result. If Bayes inversion formula is a theorem then it is not clear why it should be the basis for doing inference. What this development shows is that doing inference using entropy and of course the rules of probability, with the constraint imposed by measured data, is equivalent to the direct use of Bayes theorem to do inference. It proves Bayesian inference is just a particular case of entropic inference when the informational constraints come in the form of data. It also proves that the justification for doing Bayesian inference is the same as for entropic inference. Further note that Eqs. (8) and (9) connect the prior at resolution d to the posterior at the previous coarser scale.

APPENDIX B: RENORMALIZATION

The simplest possible renormalization can be performed by summing n variables at a finer scale d with indices $i \in I$:

$$P(J_{d-1,I}|\{J_{d,i}\}) = \delta\left(J_{d-1,I} - \frac{1}{n^{1/a}}\sum_{i=1}^{n} J_{d,i}\right),$$

where we can choose a below. Then

$$P(J_{d-1,I}) = \int \delta\left(J_{d-1,I} - \frac{1}{n^{1/a}}\sum_{i=1}^{n} J_{d,i}\right)\prod_i P(J_{d,i}|\hat{\alpha}_i,\gamma_i).$$

If the J_d variables are distributed according to a Student t distribution, Eq. (4), then Eq. (9) leads to a convolution of Student t distributions. The characteristic function or Fourier transform of the Student t distribution is given, in terms of the modified Bessel function of the second kind by

$$\Phi_J(k) = \Gamma(\gamma)2^{\gamma-1}K_\gamma\left(\sqrt{\frac{2\gamma}{\hat{\alpha}}}|k|\right)\left[\sqrt{\frac{2\gamma}{\hat{\alpha}}}|k|\right]^{\gamma}. \tag{B1}$$

For small $|k|$ is of the form

$$\Phi_J(k) = \exp\left[-\gamma^a\left(\frac{|k|}{\sqrt{\hat{\alpha}}}\right)^a\right], \tag{B2}$$

where $a \approx 2\gamma$ for $0 < \gamma \leqslant 1$ and $a = 2$ for $\gamma \geqslant 1$. It follows that

$$\Phi_{J_{d-1,I}}(k) = \prod_{i\in I}\Phi_{J_{d,i}}\left(\frac{|k|}{n^{1/a}}\right), \tag{B3}$$

and $\Phi_{J_{d-1,I}}(k) = \Phi_{J_{d,i}}(k)$ if the parameters of the distributions in the finer scale are homogeneous. Therefore, as a good starting point to determine the prior, we can consider this function to be stable under addition, and hence the parameters of the prior distributions can be inherited from the posterior at the coarser scale.

APPENDIX C: CONNECTIVITY, GRANGER CAUSALITY, AND PDC

The most popular approach to describing the connectivity between the dynamics of two time series is cross-correlation analysis (and its frequency domain counterpart: coherence) [52] despite several limitations [53]. An alternative description of connectivity is via the notion of Granger causality (GC), whose presence cannot be rejected whenever the inclusion of past observations of a time series $x_j(n)$ is significantly helpful in improving the predictability of another series $x_i(n)$ [19]. Granger causality's main property is lack of reciprocity, i.e., if $x_j(n)$ Granger causes $x_i(n)$ it does not necessarily follow that $x_i(n)$ Granger causes $x_j(n)$ in marked contrast to using correlation coefficients between time series, which are reciprocal. This feature allows exposing the direction of information flow between $x_i(n)$ and $x_j(n)$.

The most popular way of checking for the presence of Granger causality is by fitting vector autoregressive models [54] like that in Eq. (16) so that GC cannot be rejected if its estimated $a_{ij}(r)$ model coefficients that represent the influence of $x_j(n-r)$ over $x_i(n)$ turn out to be significantly different from zero [54,55]. This interaction is readily representable in the frequency domain by taking the discrete Fourier transform of each $a_{ij}(r), r = 1,\dots,p$ sequence as in Eq. (15) leading to the definition of PDC in one possible normalized representation [Eq. (14)] of the interaction from the observed $x_j(n)$ to $x_i(n)$. Direct frequency domain inference of Eq. (15) connectivity is possible [43] and its performance can be shown to be independent from the Eq. (15) normalization. Furthermore, one may also show that PDC reflects a frequency domain mutual information rate decomposition linking $x_j(n)$ to $x_i(n)$ [56]. A recent panorama of neural connectivity issues is provided in Ref. [57].

---

[1] K. Friston, Functional and effective connectivity in neuroimaging: A synthesis, Human Brain Mapping **2**, 56 (1994).

[2] L. A. Baccalá and K. Sameshima, Parcial directed coherence: A new concept in neural structure determination, Biol. Cybern. **84**, 463 (2001).

[3] K. Friston, L. Harrison, and W. Penny, Dynamic causal modeling, Neuroimage **19**, 1273 (2003).

[4] B. Schelter, J. Timmer, and M. Eichler, Assessing the strength of directed influences among neural signals using renormalized partial directed coherence, J. Neurosci. Methods **179**, 121 (2009).

[5] F. Babiloni, F. Cincotti, C. Babiloni, F. Carducci, D. Mattia, L. Astolfi, A. Basilisco, P. M. Rossini, L. Ding, Y. Ni, J. Cheng, K. Christine, J. Sweeney, and B. He, Estimation of the cortical functional connectivity with the multimodal integration of high-resolution EEG and fMRI data by directed transfer function, Neuroimage **24**, 118 (2005).

[6] K. Friston, R. Henson, C. Phillips, and J. Mattout, Bayesian estimation of evoked and induced responses, Human Brain Mapping **27**, 722 (2006).

[7] M. Kamiński, M. Ding, W. A. Truccolo, and S. L. Bressler, Evaluating causal relations in neural systems: Granger causality,

directed transfer function and statistical assessment of significance, Biol. Cybern. **85**, 145 (2001).

[8] J. Kujala, K. Pammer, P. Cornelissen, A. Roebroeck, E. Formisano, and R. Salmelin, Phase coupling in a cerebro-cerebellar network at 8-13 Hz during reading, Cereb. Cortex **17**, 1476 (2007).

[9] A. Roebroeck, E. Formisano, and R. Goebel, Mapping directed influence over the brain using Granger causality and fMRI, Neuroimage **25**, 230 (2005).

[10] L. A. Baccalá, M. Y. Alvarenga, K. Sameshima, C. L. Jorge, and L. H. Castro, Graph theoretical characterization and tracking of the effective neural connectivity during episodes of mesial temporal epileptic seizure, J. Int. Neurosci. **3**, 379 (2004).

[11] R. Kus, M. Kaminski, and K. J. Blinowska, Determination of EEG activity propagation: Pair-wise versus multichannel estimate, IEEE Trans. Biomed. Eng. **51**, 1501 (2004).

[12] L. Astolfi, F. Cincotti, D. Mattia, M. G. Marciani, L. A. Baccala, F. d. V. Fallani, S. Salinari, M. Ursino, M. Zavaglia, and F. Babiloni, Assessing cortical functional connectivity by partial directed coherence: Simulations and application to real data, IEEE Trans. Biomed. Eng. **53**, 1802 (2006).

[13] L. Astolfi, F. Cincotti, D. Mattia, M. G. Marciani, L. A. Baccala, F. de Vico Fallani, S. Salinari, M. Ursino, M. Zavaglia, L. Ding, J. C. Edgar, G. A. Miller, B. He, and F. Babiloni, Comparison of different cortical connectivity estimators for high-resolution EEG recordings, Human Brain Mapping **28**, 143 (2007).

[14] G. G. Supp, A. Schlögl, N. Trujillo-Barreto, M. M. Mler, and T. Gruber, Directed cortical information flow during human object recognition: Analyzing induced EEG gamma-band responses in brain's source space, PloS One **2**, e684 (2007).

[15] P. L. Nunez and R. Srinivasan, *Electric Fields of the Brain: The Neurophysics of EEG*, 2nd ed. (Oxford University Press, Oxford, 2006).

[16] G. Gómez-Herrero, M. Atienza, K. Egiazarian, and J. L. Cantero, Measuring directional coupling between EEG sources, Neuroimage **43**, 497 (2008).

[17] G. Nolte and K.-R. Müller, Localizing and estimating causal relations of interacting brain rhythms, Front Hum Neurosci **4**, 209 (2010).

[18] D. W. Gow, Jr., J. A. Segawa, S. P. Ahlfors, and F.-H. Lin, Lexical influences on speech perception: A Granger causality analysis of MEG and EEG source estimates, Neuroimage **43**, 6143 (2008).

[19] C. W. J. Granger, Investigating causal relations by econometric models and cross-spectral methods, Econometrica **37**, 424 (1969).

[20] E. Basar, *Memory and Brain Dynamics: Oscillations Integrating Attention, Perception, Learning, and Memory* (CRC Press, Boca Raton, 2004).

[21] D. Y. Takahashi, L. A. Baccalá, and K. Sameshima, Connectivity inference between neural structures via partial directed coherence, J. Appl. Stat. **34**, 1259 (2007).

[22] M. A. Sato, T. Yoshiota, S. Kajihara, K. Toyama, N. Goda, K. Doya, and M. Kawato, Hierarchical Bayesian estimation for MEG inverse problem, Sci. Technol. **23**, 806 (2004).

[23] S. S. Dalal, J. M. Zumer, A. G. Guggisber, M. Trumps, D. D. E. Wong, K. Sekihara, and S. S. Srikantan, MEG/EEG source reconstruction, Statistical Evaluation, and Visualisation with NUTMEG, Comput. Intell. Neurosci. **2011**, 1 (2011).

[24] R. D. Pascual-Marqui, Standardized low-resolution brain electromagnetic tomography (sLORETA): Technical details, Methods Find. Exp. Clin. Pharmacol. **24**, 5 (2002).

[25] M. Hämäläinen and R. Ilmoniemi, Interpreting magnetic fields of the brain: Minimum norm estimates, Med. Biol. Eng. Comput. **32**, 35 (1994).

[26] N. Caticha, Source localization by entropic inference and backward renormalization group priors, Entropy **17**, 2573 (2015).

[27] B. Fischl, M. I. Sereno, and A. M. Dale, Cortical surface-based analysis. I. segmentation and surface reconstruction, Neuroimage **9**, 195 (1999).

[28] S. da R. Amaral, S. R. Rabbani, and N. Caticha, Multigrid priors for a Bayesian approach to fMRI, Neuroimage **23**, 654 (2004).

[29] S. da R. Amaral, S. R. Rabbani, and N. Caticha, BOLD response analysis by iterated local multigrid priors, Neuroimage **36**, 361 (2007).

[30] B. Fischl, M. I. Sereno, and A. M. Dale, Cortical Surface-Based Analysis. II: Inflation, Flattening, and a Surface-Based Coordinate System, Neuroimage **9**, 195 (1999).

[31] D. H. Hubel and T. N. Wiesel, Shape and Arrangement of Columns in Cat's Striate Cortex, J. Physiol. **165**, 559 (1963).

[32] A. Peters, and G. J. Edward, *Cellular Components of the Cerebral Cortex* (Plenum Press, New York, 1984).

[33] A. M. Winkler, P. Kochunov, J. Blangero, L. Almasy, K. Zilles, P. T. Fox, and D. C. Glahn, Cortical thickness or grey matter volume? The importance of selecting the phenotype for imaging genetics studies, Neuroimage **53**, 1135 (2010).

[34] D. Geselowitz, On bioelectric potentials in an inhomogeneous volume conductor, Biophys. J. **7**, 1 (1967).

[35] J. C. Mosher, P. S. Lewis, and R. M. Leahy, Multiple dipole modeling and localization from spatio-temporal MEG data, IEEE Trans. Biomed. Eng. **39**, 541 (1992).

[36] J. C. Mosher, R. M. Leahy, and P. S. Lewis, EEG and MEG: forward solutions for inverse methods, IEEE Trans. Biomed. Eng. **46**, 245 (1999).

[37] T. F. Oostendorp and A. van Oosterom, Source parameter estimation in in- homogeneous volume conductors of arbitrary shape, IEEE Trans. Biomed. Eng. **36**, 382 (1989).

[38] G. Scharf, L. Dang, and C. Scharf, Electrophysiology of living organs from first principles, arXiv:1006.3453v1 (unpublished).

[39] A. Gramfort, M. Luessi, E. Larson, D. Engemann, D. Strohmeier, C. Brodbeck, L. Parkkonen, and M. Hämäläinen, MNE software for processing MEG and EEG data, Neuroimage **86**, 446 (2014).

[40] SPM8 manual, 2011, http://www.fil.ion.ucl.ac.uk/spm/doc/manual.pdf; http://fieldtrip.fcdonders.nl/

[41] A. Giffin and A. Caticha, Updating probabilities with data and moments. *Bayesian Inference and Maximum Entropy Methods in Science and Engineering*, edited by A. Mohammad-Djafari AIP Conf. Proc. **872**, 31 (2006).

[42] S. L. Marple, *Digital Spectral Analysis with Applications*, Signal Processing Series (Prentice-Hall, Upper Saddle River, 1987).

[43] L. A. Baccalá, C. S. N. Brito De, D. Y. Takahashi, and K. Sameshima, Unified asymptotic theory for all partial directed coherence forms, Phil. Trans. R. Soc. A **371**, 20120158 (2013).

[44] Further information and downloadable PDC inference software, as used here, is available from http://www.lcs.poli.usp.br/∼baccala/pdc including the programs to compute the statistical decision thresholds [21,40] used in the present work.

[45] R. Henson, J. Mattout, C. Phillips, and K. J. Friston, Selecting forward models for MEG source-reconstruction using model-evidence, Neuroimage **46**, 168 (2009).

[46] Z. A. Acar and S. Makeig, Effects of forward model errors on EEG source localization, Brain Topography **26**, 378 (2013).

[47] A. G. Guggisberg *et al.*, Localization of cortico-peripheral coherence with electroencephalography, Neuroimage **57**, 1348 (2011).

[48] K. Sekihara, S. Maneesh, and S. S. Nagarajan, Localization bias and spatial resolution of adaptive and non-adaptive spatial filters for MEG source reconstruction, Neuroimage **25**, 1056 (2005).

[49] K. Sekihara, S. Nagarajan, D. Poeppel, and A. Marantz, Performance of an MEG adaptive-beamformer technique in the presence of correlated neural activities: Effects on signal intensity and time-course estimates, IEEE Trans. Biomed. Eng. **49**, 1534 (2002).

[50] R. Henson, Y. Goshen-Gottstein, T. Ganel, L. Otten, A. Quayle, and M. Rugg, Electrophysiological and hemodynamic correlates of face perception, recognition and priming, Cereb. Cortex **13**, 793 (2003).

[51] R. Henson, E. Mouchlianitis, and K. J. Friston, MEG and EEG data fusion: Simultaneous localisation of face-evoked responses, Neuroimage **47**, 581 (2009).

[52] O. Sporns, *Networks of the Brain* (MIT Press, Cambridge, 2011).

[53] L. A. Baccalá and K. Sameshima, Overcoming the limitations of correlation analysis for many simultaneously processed neural structures, Prog. Brain Res. **130**, 33 (2001).

[54] H. Lütkepohl, *New Introduction to Multiple Time Series Analysis* (Springer, New York, 2005).

[55] C. W. J. Granger, Testing for causality: A personal viewpoint, J. Econ. Dyn. Control **2**, 329 (1980).

[56] D. Y. Takahashi, L. A. Baccalá, and K. Sameshima, Information theoretic interpretation of frequency domain connectivity measures, Biol. Cybern. **103**, 463 (2010)

[57] K. Sameshima and L. A. Baccalá, *Methods in Brain Connectivity Inference Through Multivariate Time Series Analysis* (CRC Press, Boca Raton, 2014).